

PAPER

## Magnetically active transition metal cation-substituted alumina

To cite this article: Changning Li *et al* 2019 *Nanotechnology* **31** 105703

View the [article online](#) for updates and enhancements.



**IOP | ebooks™**

Bringing together innovative digital publishing with leading authors from the global scientific community.

Start exploring the collection—download the first chapter of every title for free.

# Magnetically active transition metal cation-substituted alumina

Changning Li<sup>1</sup> , Nicholas Ku<sup>2</sup>, Yaohua Liu<sup>3</sup>, Jinbo Pan<sup>4</sup>, Binbo Chai<sup>1</sup>, Feng Hu<sup>1</sup>, Michael Kornecki<sup>2</sup>, Qimin Yan<sup>4,5</sup>, Raymond Brennan<sup>2,5</sup> and Shenqiang Ren<sup>1,5</sup> 

<sup>1</sup>Department of Mechanical and Aerospace Engineering, Department of Chemistry, Research and Education in Energy Environment and Water (RENEW) Institute, University at Buffalo, The State University of New York, Buffalo, NY 14260, United States of America

<sup>2</sup>US Army Research Laboratory, Aberdeen Proving Ground, MD 21005, United States of America

<sup>3</sup>Quantum Condensed Matter Division, Oak Ridge National Laboratory, Oak Ridge, TN 37831, United States of America

<sup>4</sup>Department of Physics, Temple University, Philadelphia, PA 19122, United States of America

E-mail: [qiminyan@temple.edu](mailto:qiminyan@temple.edu), [raymond.e.brennan.civ@mail.mil](mailto:raymond.e.brennan.civ@mail.mil) and [shenren@buffalo.edu](mailto:shenren@buffalo.edu)

Received 15 July 2019, revised 18 October 2019

Accepted for publication 21 November 2019

Published 16 December 2019



CrossMark

## Abstract

Alumina ( $\text{Al}_2\text{O}_3$ ) is one of the most widely used ceramic materials for innumerable applications, due to its unique combination of attractive physical and mechanical properties. These intrinsic properties are dictated by the numerous phases that  $\text{Al}_2\text{O}_3$  forms and its related phase transformations. Transition metal (TM) cation dopants (iron (Fe), cobalt (Co), nickel (Ni) and manganese (Mn)), even in sparse amounts, have been shown to significantly affect the phase transformation and microstructural evolution of  $\text{Al}_2\text{O}_3$ . Small concentrations of TM cation dopants have successfully been incorporated to synthesize magnetically active  $\text{Al}_2\text{O}_3$ , while reducing the  $\theta$  to  $\alpha$  phase transformation temperature by 150 °C, and maintaining the outstanding mechanical properties. In addition, first-principle calculations based on density-functional theory with hybrid functional (HSE06) and the PBE+U methods have provided a mechanistic understanding of the formation energy and magnetism of the TM-doped  $\alpha$  and  $\theta$  phases of  $\text{Al}_2\text{O}_3$ . The results reveal a potential route for phase transition regulation and external magnetic field-induced texturing of  $\text{Al}_2\text{O}_3$  ceramics.

Supplementary material for this article is available [online](#)

Keywords: phase transition, alumina, magnetically active, dopant

(Some figures may appear in colour only in the online journal)

## 1. Introduction

In recent years, cation-doped  $\text{Al}_2\text{O}_3$  has been extensively studied as an important ionic ceramic material for catalyst support [1–3], thermal-barrier coatings [4, 5], transparent armor [6, 7], and laser host materials [8], due to its excellent chemical, mechanical, and optical properties, all of which have been influenced by crystalline phases and microstructural characteristics (e.g. grain size). Dopant cations typically do not influence deformation of the crystal cell

structure, but are known to impact the sintering thermodynamic behavior and grain growth of the desired  $\text{Al}_2\text{O}_3$  phase by entering the interspace (octahedral or tetrahedral sites) and/or replacing cations of the intrinsic crystal lattice, affecting the ionic bond energy [9, 10] and grain size [11]. It has been reported that mechanical properties, such as the abrasive resistance [12], can be increased with  $\text{Al}_2\text{O}_3$  grain size reduction [13]. For dopant elements with net unpaired electrons, dopant ions can strengthen the coupling between micro-domains under external magnetic fields [14], improving the overall strength [15]. A distinct relationship between lanthanide (Ln) doping and microstructural evolution in Ln-

<sup>5</sup> Authors to whom any correspondence should be addressed

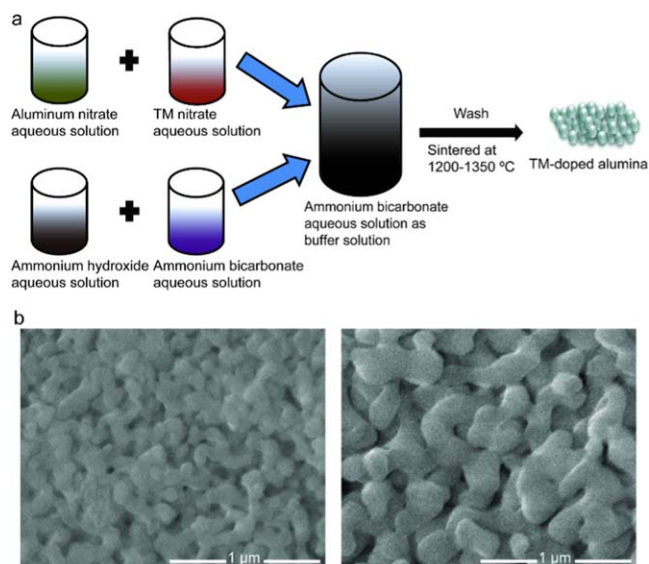


**Figure 1.** (a) Schematic representation of the TM-doped Al<sub>2</sub>O<sub>3</sub> samples preparation process. (b) SEM images of Ni-doped Al<sub>2</sub>O<sub>3</sub> under 1200 °C (left) and 1350 °C (right) respectively.

doped Al<sub>2</sub>O<sub>3</sub> has been experimentally described in our previous studies [16]. In this effort, the focus is on exploration of Al<sub>2</sub>O<sub>3</sub> doped with 3d transition metal (TM) cations, such as Fe, Co, Ni, and Mn, which have high magnetic moments, and similar radii to Al. In addition, magnetic TM dopants could potentially induce crystallographic texturing in Al<sub>2</sub>O<sub>3</sub> materials. The microstructures and physical properties of TM-doped Al<sub>2</sub>O<sub>3</sub> under different calcination temperatures have been studied with a combination of high-resolution x-ray diffraction (HRXRD), x-ray absorption near-edge structure (XANES), electron microscopy, vibrating sample magnetometry, and nano-indentation. To corroborate experimental findings, hybrid-functional based density-functional theory (DFT) calculations were also performed to aid in mechanistic understanding of phase transformations in TM-doped alumina.

## 2. Experimental section

### 2.1. Sample preparation

A wet chemical synthesis process via precipitation was utilized in a similar manner to Sanamyan *et al* [17]. The constituent elements investigated in this study were Fe, Co, Mn, and Ni. The metal salts used as cation sources for the synthesis were all commercially available products from Alfa Aesar (Haverhill, MA): aluminum nitrate nonahydrate [Al(NO<sub>3</sub>)<sub>3</sub>·9H<sub>2</sub>O] (99.999%), manganese (II) nitrate hydrate [Mn(NO<sub>3</sub>)<sub>2</sub>·xH<sub>2</sub>O] (99.999%), iron (III) nitrate nonahydrate [Fe(NO<sub>3</sub>)<sub>3</sub>·9H<sub>2</sub>O] (99.999%), cobalt (II) nitrate hexahydrate [Co(NO<sub>3</sub>)<sub>2</sub>·6H<sub>2</sub>O] (99.999%), and nickel (II) nitrate hexahydrate [Ni(NO<sub>3</sub>)<sub>2</sub>·6H<sub>2</sub>O] (99.9985%). A solution was prepared in deionized H<sub>2</sub>O with a nitrate concentration of 2.15 M. All of the TM-doped Al<sub>2</sub>O<sub>3</sub> samples referenced in this study were

prepared to form a composition with doping level around 400 ppm.

As shown in figure 1(a), acidic solutions of aluminum nitrate and TM nitrate, along with basic solutions of ammonium hydroxide (NH<sub>3</sub>·H<sub>2</sub>O) and ammonium bicarbonate (NH<sub>4</sub>HCO<sub>3</sub>) in deionized H<sub>2</sub>O, were simultaneously added dropwise into a buffer solution with pH of 7. As the four solutions were combined in the buffer, particles of doped Al<sub>2</sub>O<sub>3</sub> precursor began to precipitate out into suspension. The flow rate of the basic solution was adjusted to maintain the pH of the bath at 7 for the duration of the synthesis process. During the entire titration process, the suspension was mixed using a magnetic stir bar.

After the precipitation process was completed, the suspension was stirred overnight to allow the particles to ripen before being filtered through nitrocellulose paper. The collected particles were then dispersed in deionized H<sub>2</sub>O and filtered two times to wash off any remnant salts from synthesis. Finally, the particles were dispersed in isopropanol and filtered to aid in the drying process, before being placed in an oven at 70 °C. Once dried, the precursor powder was ground with a mortar and pestle.

### 2.2. Material characterization

HRXRD (Synchrotron 11-BM at the Advanced Photon Source (APS) of Argonne National Laboratory) was employed to examine the effect of doping on Al<sub>2</sub>O<sub>3</sub> crystalline phase composition based on the TM species and sintering temperature. The TM species doped in the alumina samples *K*-edge XANES spectra were collected using linear polarized x-rays at the undulator beamline 20-ID-C of the APS in Argonne National Laboratory. XANES spectra for TM standards used in linear combination fitting of all XANES spectra were performed under the same beamlines. The phase evolution and grain size of TM-doped Al<sub>2</sub>O<sub>3</sub> samples were further confirmed through a direct observation of the powder under an FRI Quanta450FEG SEM and TEM. The magnetization of the samples was characterized by a MircoSense EV7 high sensitivity vibrating sample magnetometer. Compressive force displacement curves and ultrafast extreme property mapping (XPM) images were measured with Hysitron TI 950 TriboIndenter/Nanoindenter and TI980 TriboIndenter with a diamond Berkovich tip. Optical transmittance of the samples was analyzed using an Agilent Model HP8453 UV-vis spectrophotometer.

## 3. Results and discussion

Of the many distinct crystalline phases of Al<sub>2</sub>O<sub>3</sub>, the α-phase, which possesses a hexagonal closed packed oxygen sub-lattice, has demonstrated remarkable hardness and been identified as the most thermodynamically stable.

All other metastable phases of Al<sub>2</sub>O<sub>3</sub> irreversibly transform to α-phase under high temperature conditions (typically above 1300 °C). The phase transition of Al<sub>2</sub>O<sub>3</sub> can follow many paths, depending on the initiating alumina precursor,

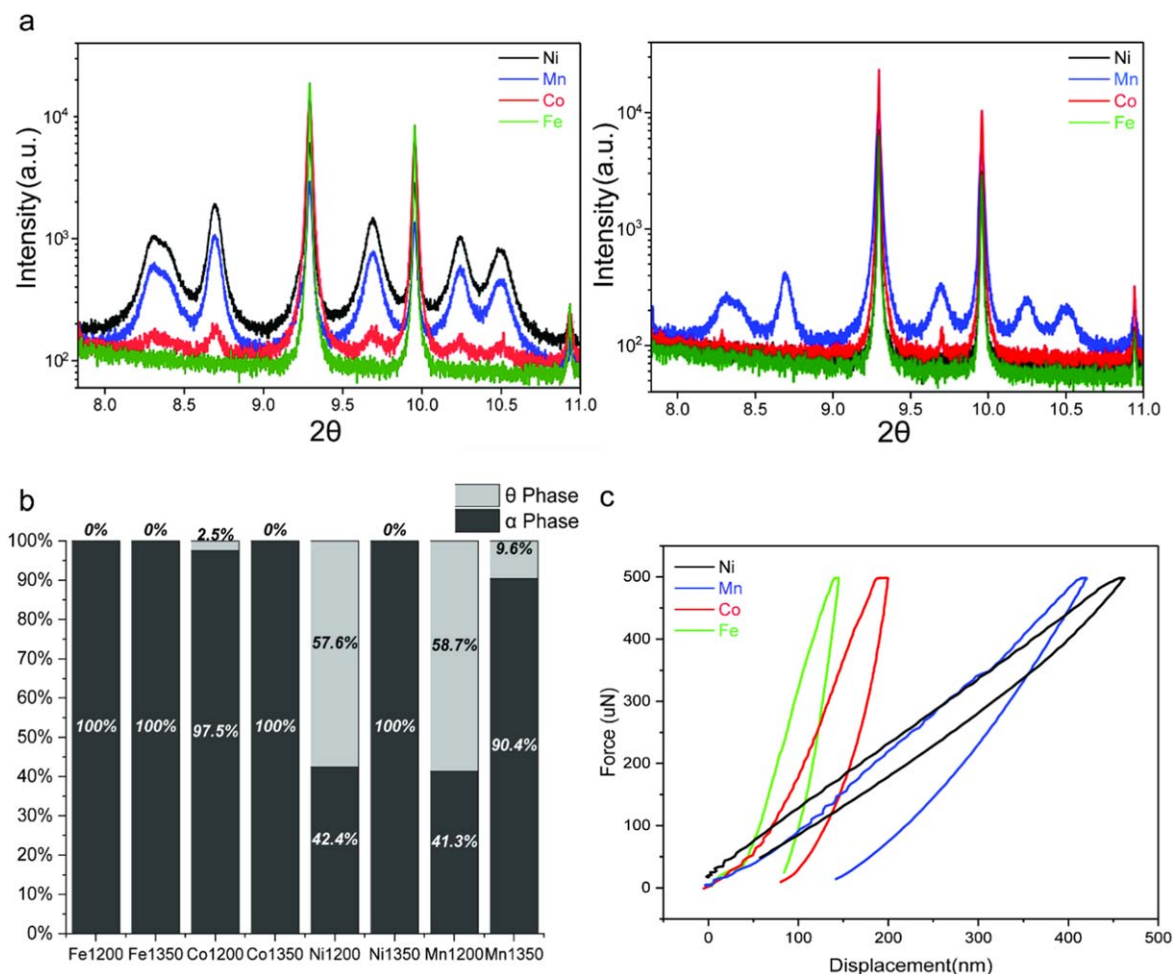


**Figure 2.** (a) HRXRD spectra of the TM-doped  $\text{Al}_2\text{O}_3$  samples calcined under 1200 °C (left) and 1350 °C (right). (b) Rietveld refinement results on the percentages of  $\alpha$ -phase and  $\theta$ -phase. (c) Compressive stress–strain curves as the rigidity measurement results on TM cation-doped  $\text{Al}_2\text{O}_3$  samples calcined under 1200 °C.

typically starting with a boehmite structure, and followed by the transition sequence of gamma ( $\gamma$ ), delta ( $\delta$ ), theta ( $\theta$ ), and alpha ( $\alpha$ ) with increasing temperature [18]. TM-doped  $\text{Al}_2\text{O}_3$  powders were synthesized following the procedures shown in figure 1(a) [12, 16]. Ammonium aluminum hydroxide carbonate ( $\text{NH}_4\text{Al}_{1-x}\text{TM}_x(\text{OH})_2\text{CO}_3$ ) was generated via an *in situ* precipitation method in an aqueous environment, and the resulting powder was dried and calcined at a set temperature in air. By precisely controlling the atomic ratios of TM dopants, the concentrations of TM species were maintained at a constant level of  $\text{TM}_{0.0007}\text{Al}_{1.9993}\text{O}_3$  (ca. 400 ppm), to avoid potential formation of TM aluminate and/or oxide phases. A bi-modal size distribution was observed in all TM-doped  $\text{Al}_2\text{O}_3$  samples (as shown in figure 1(b), taking Ni-doped  $\text{Al}_2\text{O}_3$  as an example, and figure S1 is available online at [stacks.iop.org/NANO/31/105703/mmedia](https://stacks.iop.org/NANO/31/105703/mmedia)), which indicated the presence of a mixture of crystalline phases in the powder samples. It was observed that the resulting crystalline phase composition did not solely rely on the dopant species, but was influenced by the calcination temperatures as well. HRXRD measurements were performed to confirm the crystalline phase compositions. In order to compare the effect of the dopant species on crystalline phase transformations ( $\theta$  to

$\alpha$ -phase transition), doped  $\text{Al}_2\text{O}_3$  was calcined under different temperatures below 1350 °C (the characteristic phase-transition temperature of pure  $\text{Al}_2\text{O}_3$ ). It should be noted that when the calcination temperature was increased to 1350 °C,  $\text{Al}_2\text{O}_3$  with various dopants (with the exception of the Mn-doped samples) could be converted to  $\alpha$ -phase.

As evidenced in the corresponding HRXRD spectra (figure 2(a)), there were no notable  $\theta$ -phase diffraction signals in the Fe-, Co-, and Ni-doped  $\text{Al}_2\text{O}_3$ . These spectra were consistent with the size distribution of doped  $\text{Al}_2\text{O}_3$ , where the  $\alpha$ -phase dominated grains were represented by the uniform spherical shapes and dimensions. When the calcination temperature was decreased to 1200 °C, the Fe- and Co-doped  $\text{Al}_2\text{O}_3$  demonstrated homogeneous and uniform shapes, in accordance with the XRD spectra. The Co-doped  $\text{Al}_2\text{O}_3$  prepared at 1200 °C suggested a notably larger portion of  $\alpha$ -crystalline phase, while no  $\theta$ -phase was observed in the Fe-doped  $\text{Al}_2\text{O}_3$ . All  $\theta$ -phase transitioned into  $\alpha$ -phase for the Fe-doped  $\text{Al}_2\text{O}_3$ , indicating a reduction in phase transition temperature by 150 °C, compared to that of pure  $\text{Al}_2\text{O}_3$ . In addition, the x-ray diffraction patterns confirmed that the crystalline structure of  $\text{Al}_2\text{O}_3$  was not affected by doping. Based on these observations, all of the spectra were

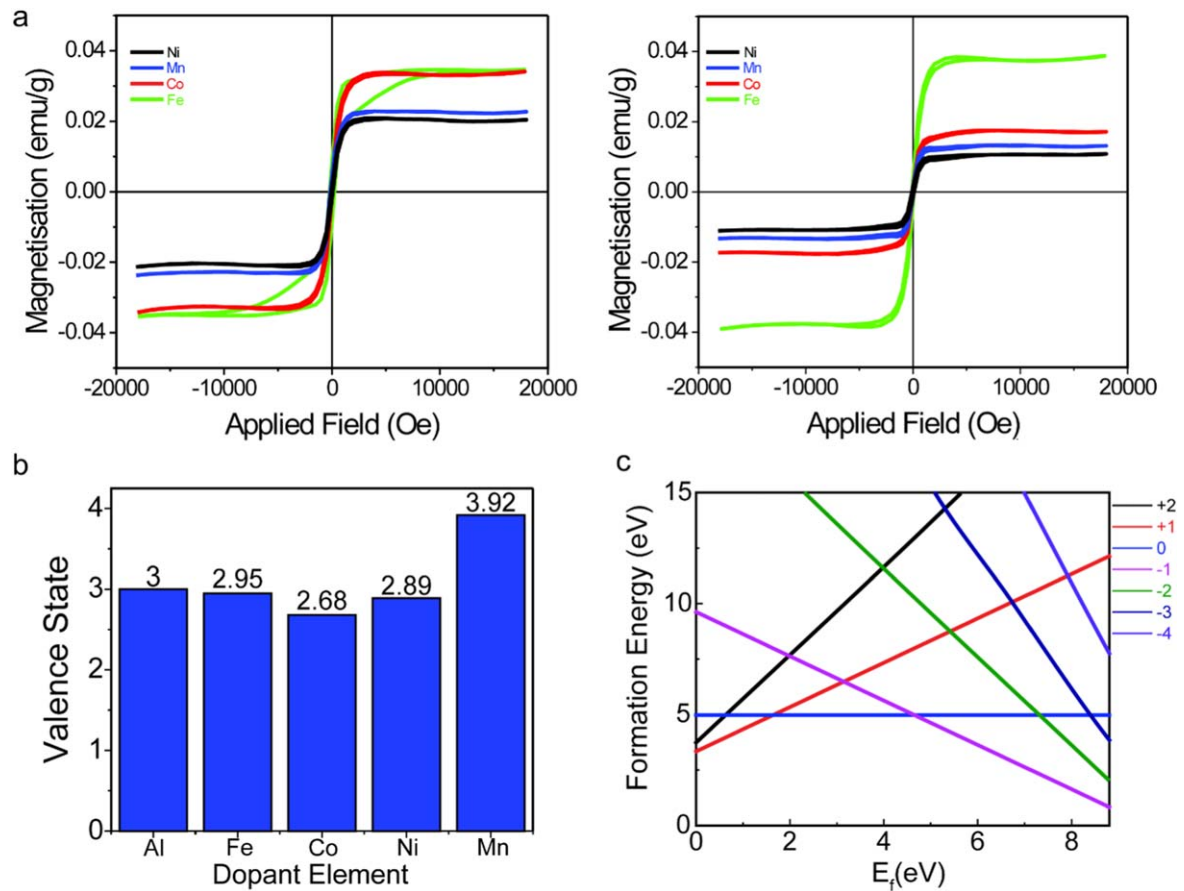


**Figure 3.** (a) MH loops of TM cation-doped alumina samples calcined under 1200 °C (left) and 1350 °C (right). (b) Valence states of TM cation dopant in the  $Al_2O_3$  based on XANES spectra calculated from LCF with corresponding standard samples. (c) Formation energies as a function of Fermi level ( $E_f$ ) for Fe-doped  $Al_2O_3$  samples.

**Table 1.** The calculated energy difference between  $\theta$  and  $\alpha$  phases of pure  $Al_2O_3$  and Fe-doped  $Al_2O_3$  systems in supercells containing 48 aluminum and 72 oxygen atoms.

DFT Methods	Energy difference ( $dE = (E_{tot}(\theta) - E_{tot}(\alpha))$ ) (eV)	
	Pure $Al_2O_3$	Fe-doped $Al_2O_3$
HSE06	3.000	4.881
PBE+U	1.048	1.522

comparatively studied and analyzed quantitatively by Rietveld refinement (figure 2(b)). Rietveld refinement was also utilized to obtain the crystallite phase composition for TM-doped  $Al_2O_3$ . At the calcination temperature of 1350 °C, all  $\theta$ -phase was transformed to  $\alpha$ -phase in the Co- and Ni-doped samples, while 9.6% of  $\theta$ -phase remained in the Mn-doped  $Al_2O_3$  sample. In addition, the average grain sizes in the Co-, Ni- and Mn-doped  $Al_2O_3$  samples were enlarged as a result of the  $\theta$ - to  $\alpha$ -phase transition. All of the particles were approximately the same size before sintering (figure S2). Another noteworthy feature was that there were no detectable signals from TM aluminate and/or oxide phases, based on x-ray Diffraction spectra and energy dispersive x-ray imaging

and analysis (figures S3–S10). Furthermore, the ratio of  $\alpha$ -phase was consistent with the mechanical properties, as indicated by nano-indentation testing, in which an external load was applied through a nano-indenter tip on the sample surface under force-control mode, resulting in a maximum force of 500  $\mu$ N applied to the sample (figure 2(c)). The displacement distances of the  $Al_2O_3$  samples increased with the ratio of  $\theta$ -phase. The nano-indentation test, along with XPM (figure S11), and optical characterization (figure S12) suggested that the structural properties of  $Al_2O_3$  were not influenced by the introduction of TM cations.

The magnetic hysteresis loops of TM-doped  $Al_2O_3$  demonstrated paramagnetic properties (figure 3(a)). The saturation magnetization ( $M_s$ ) of TM-doped  $Al_2O_3$  was matched with the extra-nuclear electron configuration of doping elements collected from XANES for Fe, Co, Mn and Ni. Based on the valence state characterization of TM-doped  $Al_2O_3$  calcined at 1350 °C (figure 3(b)), according to the Pauli exclusion principle and Hund's Rules, the Fe cation indicated 4.950 unpaired electrons, while Co, Mn and Ni, indicated 3.676, 3.083 and 2.892 unpaired electrons, respectively. The same relative magnitude order was observed in TM-doped  $Al_2O_3$  calcined at 1200 °C. It should be noted that the Co, Mn, and Ni valence states in the calcined samples were higher than those of the chemicals selected as

precursors. Oxidization occurred during the preparation process except for the Fe-doped samples, as  $\text{Co}^{2+}$ ,  $\text{Ni}^{2+}$  and  $\text{Mn}^{2+}$  were oxidized to +2.676, +2.892, and +3.917, respectively. The spin density distributions and net magnetic moments did not solely depend on the unpaired electrons of the dopant elements, but were also affected by the coupling interaction intensities of atomic magnetic moment in the solid TM-doped  $\text{Al}_2\text{O}_3$  material. As such, regarding the trace dopant concentration in  $\text{Al}_2\text{O}_3$ , it may imply that the coupling interaction intensities of atomic magnetic moments in the TM cations were similar to that of hydrated cations in an aqueous solution. Taking into consideration that pure  $\text{Al}_2\text{O}_3$  is diamagnetic, the paramagnetic signals from low TM concentrations in doped  $\text{Al}_2\text{O}_3$ , especially for Fe-doped at 1200 °C, indicating the possibility of magnetic field texturing. In order to gain insight into the notable reduction of phase transition temperatures in Fe-doped  $\text{Al}_2\text{O}_3$  samples, the formation energies of the  $\theta$ - and  $\alpha$ -phases were calculated as a function of the Fermi levels ( $E_F$ ) using first-principles computations (figure 3(c)). The formation energy of the Fe impurity in  $\text{Al}_2\text{O}_3$  at a charge defect  $q$  was calculated using DFT with the hybrid functional:

$$E^f = E_{\text{tot}} - E(\text{Al}_2\text{O}_3) + \mu_{\text{Al}} - \mu_{\text{Fe}} + q(E_F + \varepsilon_v) + \Delta q,$$

where  $E_{\text{tot}}$  is the total energy of the supercell containing Fe-doped  $\text{Al}_2\text{O}_3$ ,  $E(\text{Al}_2\text{O}_3)$  is the total energy of a perfect crystal in the same supercell,  $q$  is the charge state of the point defect,  $\mu_{\text{Al}}$  and  $\mu_{\text{Fe}}$  are chemical potentials of Al and Fe atoms (−4.37 and −13.05 eV, obtained from the total energies of elemental Al and Fe, respectively),  $E_F$  is the Fermi level, and  $\varepsilon_v$  is the energy of valence band maximum. Note that the choice of chemical potentials does not affect the positions of thermodynamic charge-state transition levels. It was clear that substitutional Fe impurities could exist in  $\text{Al}_2\text{O}_3$  samples at −, 0, and + charge states, depending on the Fermi level of the samples. The magnetic moment on the Fe atom was calculated as 1 Bohr magneton for neutral impurity and 2 Bohr magnetons for dopants in the—charge state. For the case of neutral impurities, the relative energy difference between the two phases was calculated, and it was observed that Fe-doping could further increase the energy difference and effectively stabilize the  $\alpha$ -phase (table 1). This conclusion was confirmed by two computational methods, including the HSE06 and PBE+U methods, as shown in table 1. The temperature effects on the total energy change due to entropy were not included in the calculations, as they were known to reduce the energy differences between the two phases, but this would not influence the conclusion on relative phase stability either way.

#### 4. Conclusion

It was demonstrated that sintering of  $\text{Al}_2\text{O}_3$  could be significantly influenced by the presence of transition elements, providing insight into how phase transformations and

microstructural evolution varied with dopant species (based on systematic studies of Fe, Ni, Co, and Mn cation-doped  $\text{Al}_2\text{O}_3$  materials). This was observed during the heat treatment process, and verified by first-principles computations. A relationship between the unpaired electrons of the doped TM cations and the macroscopic properties was reported experimentally. By adding a sparse amount of 3d TM dopants, diamagnetic  $\text{Al}_2\text{O}_3$  became magnetically active, showing the potential of controlling the texture of bulk  $\text{Al}_2\text{O}_3$  ceramics in the presence of external magnetic fields without sacrificing mechanical and optical properties.

#### Acknowledgments

Financial support was provided by the US Army Research Office supports SR under Award W911NF-18-2-0202. Use of the Advanced Photon Source (11-BM) at Argonne National Laboratory was supported by the US Department of Energy, Office of Science, Office of Basic Energy Sciences, under Contract No. DE-AC02-06CH11357. Work at ORNL was supported by the Division of Scientific User Facilities of the Office of Basic Energy Sciences (BES), US Department of Energy (DOE). The research reported in this document was performed in connection with contract/instrument W911QX-16-D-0014 with the US Army Research Laboratory. The views and conclusions contained in this document are those of Service Engineering and the US Army Research Laboratory. Citation of manufacturer's or trade names does not constitute an official endorsement or approval of the use thereof. The US Government is authorized to reproduce and distribute reprints for Government purposes notwithstanding any copyright notation hereon.

#### ORCID iDs

Changning Li  <https://orcid.org/0000-0002-2216-3594>  
Shenqiang Ren  <https://orcid.org/0000-0002-9987-3316>

#### References

- [1] Peterson E J *et al* 2014 Low-temperature carbon monoxide oxidation catalysed by regenerable atomically dispersed palladium on alumina *Nat. Commun.* **5** 4885
- [2] Garbarino G *et al* 2018 Ethanol and diethyl ether catalytic conversion over commercial alumina and lanthanum-doped alumina: reaction paths, catalyst structure and coking *Appl. Catalysis B* **236** 490–500
- [3] Toyao T *et al* 2018 Catalytic NO–CO Reactions over La- $\text{Al}_2\text{O}_3$  Supported Pd: promotion effect of La *Chem. Lett.* **47** 1036–9
- [4] Matsudaira T *et al* 2011 Oxygen permeability in cation-doped polycrystalline alumina under oxygen potential gradients at high temperatures *Acta Mater.* **59** 5440–50
- [5] Evans A G *et al* 2001 Mechanisms controlling the durability of thermal barrier coatings *Prog. Mater. Sci.* **46** 505–53
- [6] Grujicic M, Bell W and Pandurangan B 2012 Design and material selection guidelines and strategies for transparent armor systems *Mater. Des.* **34** 808–19

- [7] Salem J A 2013 Transparent armor ceramics as spacecraft windows *J. Am. Ceram. Soc.* **96** 281–9
- [8] Penilla E H *et al* 2018 Gain in polycrystalline Nd-doped alumina: leveraging length scales to create a new class of high-energy, short pulse, tunable laser materials *Light: Sci. Appl.* **7** 33
- [9] Andersson J M *et al* 2005 *Ab initio* calculations on the effects of additives on alumina phase stability *Phys. Rev. B* **71** 014101
- [10] Mortazavi N *et al* 2018 Interplay of water and reactive elements in oxidation of alumina-forming alloys *Nat. Mater.* **17** 610–7
- [11] Pint B, Martin J A and Hobbs L 1993 18 O/SIMS characterization of the growth mechanism of doped and undoped  $\alpha$ -Al<sub>2</sub>O<sub>3</sub> *Oxid. Met.* **39** 167–95
- [12] Rainforth W 2004 The wear behaviour of oxide ceramics—a review *J. Mater. Sci.* **39** 6705–21
- [13] Krell A *et al* 2003 Transparent sintered corundum with high hardness and strength *J. Am. Ceram. Soc.* **86** 12–8
- [14] Nykwest E C *et al* 2018 Magnetic and energetic properties of transition metal doped alumina *J. Phys.: Condens. Matter* **30** 395801
- [15] Li Q *et al* 2015 Rise and fall of ferromagnetism in O-irradiated Al<sub>2</sub>O<sub>3</sub> single crystals *J. Appl. Phys.* **117** 233904
- [16] Patel K *et al* 2017 Structural effects of lanthanide dopants on alumina *Sci. Rep.* **7** 39946
- [17] Sanamyan T *et al* 2013 Spectroscopic properties of Er<sup>3+</sup>-doped  $\alpha$ -Al<sub>2</sub>O<sub>3</sub> *Opt. Mater.* **35** 821–6
- [18] Wefers K and Misra C 1987 Oxides and hydroxides of aluminum (report) *Aluminum Co. Am.* **92** 1987